

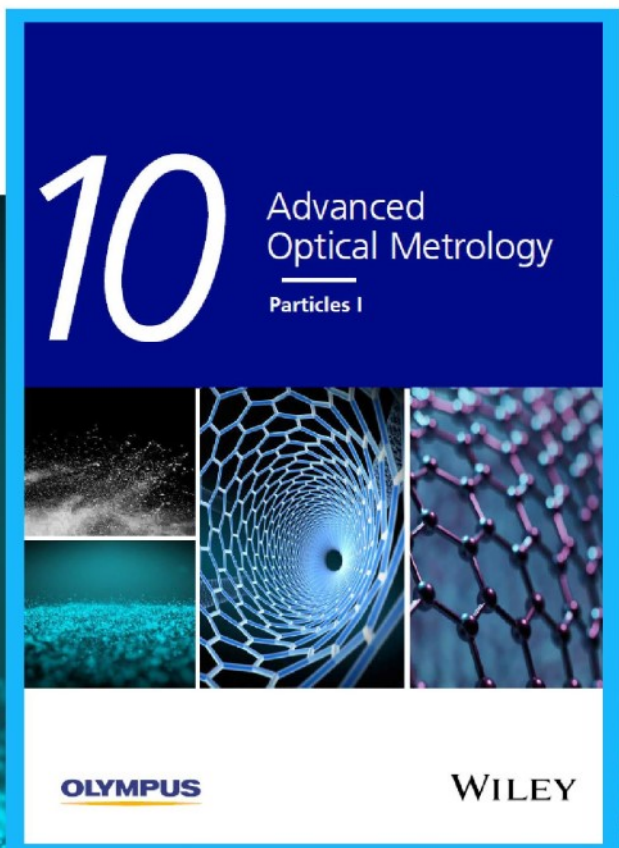


# Particles I

Access the latest eBook →

Particles: Unique Properties,  
Uncountable Applications

**Read the latest eBook and  
better your knowledge with  
highlights from the recent  
studies on the design and  
characterization of micro-  
and nanoparticles for  
different application areas.**



**Access Now**

This eBook is sponsored by

**OLYMPUS**

**WILEY**

# A Multi-Scale Approach for Modeling the Optical Response of Molecular Materials Inside Cavities

Benedikt Zerulla, Marjan Krstić, Dominik Beutel, Christof Holzer, Christof Wöll, Carsten Rockstuhl, and Ivan Fernandez-Corbaton\*

The recent fabrication advances in nanoscience and molecular materials point toward a new era where material properties are tailored *in silico* for target applications. To fully realize this potential, accurate and computationally efficient theoretical models are needed for: a) the computer-aided design and optimization of new materials before their fabrication; and b) the accurate interpretation of experiments. The development of such theoretical models is a challenging multi-disciplinary problem where physics, chemistry, and material science are intertwined across spatial scales ranging from the molecular to the device level, that is, from ångströms to millimeters. In photonic applications, molecular materials are often placed inside optical cavities. Together with the sought-after enhancement of light-molecule interactions, the cavities bring additional complexity to the modeling of such devices. Here, a multi-scale approach that, starting from *ab initio* quantum mechanical molecular simulations, can compute the electromagnetic response of macroscopic devices such as cavities containing molecular materials is presented. Molecular time-dependent density-functional theory calculations are combined with the efficient transition matrix based solution of Maxwell's equations. Some of the capabilities of the approach are demonstrated by simulating surface metal-organic frameworks -in-cavity and J-aggregates-in-cavity systems that have been recently investigated experimentally, and providing a refined understanding of the experimental results.

## 1. Introduction and Summary

The importance of materials in our civilizations can hardly be overstated. Stone, bronze, and iron lend their names to successive technological periods from the past, which lasted millions, thousands, and hundreds of years, respectively. The rate at which we engineer new materials is currently accelerating to awe-inspiring speeds. Advances in nanoscience and material science point toward a new era where materials with unprecedented properties will be tailor-made for target applications. Molecular material science pursues the old alchemist goal: Combining known elementary components to produce a new material whose properties are either unprecedented or much enhanced from those of previously existing materials. A notable class of molecular materials are metal-organic frameworks (MOF) and their flat realizations, surface MOF (SURMOF).<sup>[1,2]</sup> Such materials are made by growing scaffold-like crystalline structures formed by metallic ions and organic molecules. Some envisioned optical applications of molecular materials are


enhancement of: luminescence,<sup>[3]</sup> second harmonic generation,<sup>[4]</sup> Raman scattering,<sup>[5]</sup> infrared sensing,<sup>[6–8]</sup> and photon upconversion.<sup>[9]</sup>

To fully realize their potential, the spectacular advances in fabrication techniques need to be matched by accurate and computationally efficient theoretical models. On the one hand, such models should underpin the computer-aided design of new materials avoiding costly experimental comparisons of different alternatives as much as possible. On the other hand, the theoretical tools should support the analysis and interpretation of experimental data. The multi-scale and multi-disciplinary character of the problem renders the theory development very challenging. Physics and chemistry are intertwined across spatial scales ranging from ångströms to millimeters.<sup>[10]</sup> For example, there is a huge scale gap between the molecular unit cells of a MOF scaffold ( $\approx 1$  nm), and macroscopic systems such as MOF films that are hundreds of nanometers long in each spatial dimension. Additional complexity is added when the materials are placed inside an optical cavity for enhancing the light-matter interaction. The cavity modes are yet another

B. Zerulla, C. Rockstuhl, I. Fernandez-Corbaton  
Institute of Nanotechnology  
Karlsruhe Institute of Technology (KIT)  
D-76344 Eggenstein-Leopoldshafen, Germany  
E-mail: ivan.fernandez-corbaton@kit.edu

M. Krstić, D. Beutel, C. Holzer, C. Rockstuhl  
Institute of Theoretical Solid State Physics  
Karlsruhe Institute of Technology (KIT)  
D-76131 Karlsruhe, Germany

C. Wöll  
Institute of Functional Interfaces  
Karlsruhe Institute of Technology (KIT)  
D-76344 Eggenstein-Leopoldshafen, Germany

 The ORCID identification number(s) for the author(s) of this article can be found under <https://doi.org/10.1002/adma.202200350>.

© 2022 The Authors. Advanced Materials published by Wiley-VCH GmbH. This is an open access article under the terms of the Creative Commons Attribution-NonCommercial-NoDerivs License, which permits use and distribution in any medium, provided the original work is properly cited, the use is non-commercial and no modifications or adaptations are made.

DOI: 10.1002/adma.202200350

degree of freedom amenable to optimization beyond Fabry-Perot configurations,<sup>[6–8]</sup> and, when the interaction is strong enough, hybrid light-matter modes known as polaritons will form inside the cavity: The optical properties of the joint system can differ significantly from the separate responses of cavity and materials.<sup>[10–19]</sup> The choice of MOFs as active materials inside the cavities is motivated by the crystallinity and porosity of this class of reticular compounds, which makes possible a straightforward experimental characterization using X-ray diffraction methods as well as a tuning of the dielectric constant inside the cavity by loading the MOFs with small molecules. Hybrid light-matter states have also been observed in MOFs placed on a plasmonic nanoparticle lattice<sup>[20]</sup> and even in molecular films on top of substrates.<sup>[21]</sup>

In this article, we present a multi-scale approach for computing the electromagnetic response of devices containing molecular materials starting from ab initio quantum mechanical molecular simulations. We use state-of-the-art density functional theory (DFT) calculations<sup>[22]</sup> on the molecular side and transition matrix (T-matrix) based methods on the Maxwell side.<sup>[23]</sup> These two sides are connected by a recently established link between quantum mechanical molecular models and rigorous Maxwell scattering theory.<sup>[24]</sup> The T-matrix methodology,<sup>[25,26]</sup> which is very efficient for periodic systems,<sup>[23,27,28]</sup> allows then to efficiently compute the optical properties of periodic molecular films of arbitrary thickness. Amorphous molecular materials can also be simulated by deriving their effective material properties from quantum mechanical simulations. Both kinds of molecular materials, crystalline and amorphous, can be simulated as isolated films, on top of a substrate, or inside a planar optical cavity. We use the approach to analyze the absorption of optical cavities formed by silver mirrors, and filled with either a crystalline MOF film, or a random mixture of J-aggregates in a polymer embedding. The SURMOF simulations show effects due to the anisotropy of the molecular material. The results also show that the two largest absorption peaks observed in the measurements of a SURMOF-in-cavity system<sup>[11]</sup> belong to two different Fabry-Perot modes, while the two peaks observed for a J-aggregate-in-cavity system<sup>[29]</sup> belong to the same mode. It is found that the reason for this qualitative difference is the larger concentration of molecules in the SURMOF system, which causes a more pronounced bending of the mode lines, and produces two effects when scanning the frequency at a fixed cavity thickness: An increase in the energy difference between two peaks of the same mode, and an increased possibility of detecting peaks belonging to two different modes. The multi-scale approach presented here can be used for the computer-aided design and optimization of the optical properties of devices containing molecular materials, and also for the interpretation of experimental measurements. We also foresee that the ability to simulate complex optical cavities with complex molecular materials can be of help in the booming field of polaritonic chemistry. While a full theoretical understanding of the mechanisms behind polaritonic chemistry is still not available, there is a growing consensus that a multi-scale theoretical approach where the modes of the joint cavity together with molecules system are realistically considered is an important piece of the puzzle.<sup>[10,30,31]</sup>

The article is organized as follows. First, Section 2 provides an overview of the theoretical tools that underpin our multi-scale methodology. Then, Section 3 contains a step-by-step explanation of how the optical properties of devices made from molecular materials can be computed from ab initio quantum mechanical molecular simulations. A particular example of a SURMOF-filled cavity is used for illustrating the discussion. The results of the simulation of the SURMOF-in-cavity system are then further analyzed in Section 4. In Section 5, a system consisting of randomly oriented J-aggregates in an optical cavity is investigated. Section 6 contains a brief discussion of the limitations of our approach. Finally, Section 7 contains the concluding remarks and the outlook.

## 2. Theoretical Tools

### 2.1. T-Matrix Formalism

The T-matrix formalism was introduced by Waterman<sup>[25]</sup> and is nowadays a popular tool in physics and engineering.<sup>[26]</sup> The T-matrix of a scatterer relates the fields of an incident electromagnetic wave to the fields of the scattered electromagnetic wave.

The electric field outside a single scatterer in frequency domain can be expressed as an expansion in multipolar fields

$$\mathbf{E}(\mathbf{r}) = \sum_{l=1}^{\infty} \sum_{m=-l}^l \left( a_{lm,N} \mathbf{N}_{lm}^{(1)}(k_h, \mathbf{r}) + a_{lm,M} \mathbf{M}_{lm}^{(1)}(k_h, \mathbf{r}) + p_{lm,N} \mathbf{N}_{lm}^{(3)}(k_h, \mathbf{r}) + p_{lm,M} \mathbf{M}_{lm}^{(3)}(k_h, \mathbf{r}) \right) \quad (1)$$

In Equation (1),  $k_h = \omega \sqrt{\epsilon_h(\omega) \mu_h(\omega)}$  is the wave number of the host material with  $\epsilon_h(\omega)$  the permittivity and  $\mu_h(\omega)$  the permeability of the host material at the considered frequency.  $\mathbf{N}_{lm}^{(1)}(k_h, \mathbf{r})$  and  $\mathbf{M}_{lm}^{(1)}(k_h, \mathbf{r})$  are vector spherical waves of well-defined parity, which correspond to transverse magnetic (TM) and transverse electric (TE) modes<sup>[23,24]</sup> for regular waves.  $\mathbf{N}_{lm}^{(3)}(k_h, \mathbf{r})$  and  $\mathbf{M}_{lm}^{(3)}(k_h, \mathbf{r})$  are the corresponding scattered waves. In practice, the multipolar order  $l$  must be bounded by some maximum value  $l_{\max}$ , which should be chosen to sufficiently describe the response of the scatterer. The T-matrix  $\mathbf{T}$  relates the expansion coefficients of the incident wave,  $a_{lm,N}$  and  $a_{lm,M}$ , to the expansion coefficients of the scattered wave  $p_{lm,N}$  and  $p_{lm,M}$ . Arranging the respective expansion coefficients in column vectors  $\mathbf{a}$  and  $\mathbf{p}$ , their relationship is

$$\mathbf{p} = \mathbf{T} \mathbf{a} \quad (2)$$

The T-matrix contains all the information of the linear response of an object to incident electromagnetic radiation.

The computation of the T-matrix for an individual object requires a model for the light-matter interaction. Most commonly, the model is the material constitutive relations in the macroscopic Maxwell equations. Yet, the interaction of light with single molecules and molecular clusters cannot be described in such a way. Very recent work<sup>[24]</sup> shows that quantum mechanical simulations of molecules under the perturbation of electromagnetic fields can be used to obtain the

T-matrix of molecules. The  $6 \times 6$  complex dipole polarizability matrix of a molecular unit determined using ab initio quantum mechanical methods, such as time-dependent DFT (TD-DFT), can be used to construct its dipolar T-matrix ( $l_{\max} = 1$ )

$$\begin{pmatrix} \mathbf{T}_{\text{NN}} & \mathbf{T}_{\text{NM}} \\ \mathbf{T}_{\text{MN}} & \mathbf{T}_{\text{MM}} \end{pmatrix} = \frac{ic_h Z_h k_h^3}{6\pi} \begin{pmatrix} \mathbf{C}(\alpha_{ee})\mathbf{C}^{-1} & \mathbf{C}(-i\alpha_{em}/Z_h)\mathbf{C}^{-1} \\ \mathbf{C}(i\alpha_{me}/c_h)\mathbf{C}^{-1} & \mathbf{C}(\alpha_{mm}/(c_h Z_h))\mathbf{C}^{-1} \end{pmatrix} \quad (3)$$

Except for  $\mathbf{C}$ , all quantities are generally frequency dependent, but the frequency  $\omega$  is not written explicitly as argument. In Equation (3),  $\mathbf{C}$  is a unitary matrix converting an object from the Cartesian basis to the spherical basis,  $c_h = 1/\sqrt{\epsilon_h \mu_h}$  is the speed of light in the surrounding achiral medium, and  $Z_h = \sqrt{\mu_h/\epsilon_h}$  is the wave impedance.<sup>[24]</sup> We emphasize that the  $\alpha_{vw}$  are  $3 \times 3$  complex matrices, allowing for anisotropic responses of the molecule(s). In Equation (2), the T-matrix is expressed in the basis of well-defined parity. Please note that the computations of multi-scattering between multiple objects are done with the T-matrix in helicity basis instead of parity basis. The helicity basis is more convenient when considering chiral scatterers, and also for periodic systems.<sup>[23]</sup> Parity basis refers to the expansion in modes of well-defined parity, which in the case of multipoles coincide with TE and TM modes. Helicity basis refers to the expansion in modes of well-defined helicity, which are linear combinations of TE and TM modes (Section 2.4 in ref. [32]), and whose plane wave decomposition only contain plane waves of one polarization handedness. The transfer from the T-matrix expressed in the basis of well-defined parity in Equation (3) to the T-matrix expressed in the basis of well-defined helicity can be achieved with simple matrix multiplications.<sup>[24]</sup>

The computation of the T-matrix of a composite system from the T-matrices of its constituents is numerically efficient. It is particularly efficient if the composite system is a periodic repetition of a given unit cell described by a T-matrix. When considering a scatterer with a known T-matrix inside a 2D lattice, the multi-scattering between the objects has to be included. The multi-scattering between the objects is computed for the illumination with a plane wave. The expansion coefficients  $\mathbf{p}_{0,\text{tot}}$  of the total field scattered by an object at the origin of the lattice are related to the expansion coefficients of the primary incident field  $\mathbf{a}_0$  in the following way<sup>[23]</sup>

$$\mathbf{p}_{0,\text{tot}} = \left( 1 - \mathbf{T} \sum_{\mathbf{R} \neq 0} \mathbf{C}^{(3)}(-\mathbf{R}) e^{i\mathbf{k}_\parallel \cdot \mathbf{R}} \right)^{-1} \mathbf{T} \mathbf{a}_0 \quad (4)$$

Here,  $\mathbf{R}$  is a lattice point,  $\mathbf{C}^{(3)}(-\mathbf{R})$  is a matrix consisting of translation coefficients for vector spherical waves, and  $\mathbf{k}_\parallel$  is the tangential component of the wave-vector of the primary illuminating plane wave. The objects in the lattice can be dielectric and/or metallic particles, or the molecular unit cells of a MOF. The T-matrix of such a molecular unit is obtained by quantum mechanical calculations (see Section 2.3), which, together with Equation (4) are the bases for simulating periodic molecular materials such as SURMOFs. For example, in a procedure implemented in the in-house developed mul-

tilayered periodic general mie method (mpGMM),<sup>[23]</sup> an arbitrary number of stacked SURMOF-2 sheets can be simulated very efficiently by first solving the multi-scattering problem inside a 2D lattice using Equation (4), and then computing the interaction between stacked 2D lattices. The SURMOF-2 type subgroup of crystalline SURMOFs exhibits an isorecticular structure yielding planar sheets of a crystalline material with fourfold symmetry, held together by strong bonds between metallic centers and linkers along two directions. The 3D structure is achieved by stacking planar sheets of the material along the third direction, which are coordinated only through weaker van der Waals interactions between neighboring 2D sheets.<sup>[33]</sup> In contrast, conventional MOFs/SURMOFs usually exhibit a 3D periodic structure with metallic centers coordinated to organic linkers by strong carboxylate/metal-bonds in all three directions. Conventional MOFs/SURMOFs can be similarly simulated in mpGMM. Besides lattices, the system to be studied with mpGMM can also include homogeneous and isotropic slabs of chiral or achiral materials, which can be used to model substrates and planar cavity mirrors, for example (see Figure 2). A film of non-crystalline amorphous molecular material can be included as a homogeneous and isotropic slab, whose effective material constitutive relations are derived from quantum mechanical simulations (see Sections 2.4 and 5). The cavity mirrors can also be fancier arrays of dielectric particles such as silicon disks.<sup>[6–8]</sup> Finally, the transmittance, reflectance, absorption, etc., of a given system and the electric and magnetic fields in the system can be calculated. This allows, on the one hand, to predict experimental measurements, and on the other hand, becomes a valuable tool for computer-aided design.

## 2.2. Cavity Mode Lines

Many experiments study the optical response of planar cavities filled with molecular materials. The modal equation for such systems will be derived here assuming that the illumination direction is perpendicular to the plane of the cavity mirrors, and that the response of the molecular material can be approximately assumed to be isotropic and homogeneous. The isotropic and homogeneous conditions are typically met by amorphous molecular materials. While crystalline materials such as SURMOFs are homogeneous, imposing isotropy is a simplification that leads to a simple modal equation. It will be seen later that such simplification still produces very satisfactory results. Section 2.4 explains how the effective isotropic material parameters are derived from quantum-mechanical simulations in both the amorphous and crystalline cases.

The modal lines of a cavity formed by two planar mirrors sandwiching an isotropic and homogeneous medium can be found by using the phase-matching condition for the coherent build-up of a mode upon consecutive reflections of the internal faces of the cavity mirrors:

$$2 | \text{Real} \{ k_z(\omega) \} | L + \phi_1(\omega) + \phi_2(\omega) = 2\pi l \quad (5)$$

where  $k_z(\omega)$  is the component of the wave-vector normal to the mirror planes,  $\omega$  is the angular frequency of the illumination,  $L$

is the cavity length in the z-dimension,  $\phi_1(\omega)$  and  $\phi_2(\omega)$  are the phases of the reflection coefficients in each of the two mirrors, and  $l$  is an integer that labels the mode number. For excitation with normal incidence, we have that  $|\text{Real}\{k_z(\omega)\}| = \frac{\omega \text{Real}\{n_s(\omega)\}}{c_0}$ , where  $n_s(\omega)$  is the refractive index of the medium inside the cavity, and  $c_0 = 1/\sqrt{\epsilon_0\mu_0}$ , where  $\epsilon_0$  and  $\mu_0$  are the vacuum permittivity and permeability, respectively. Then, we can isolate  $L$  as:

$$L(\omega) = \frac{c_0}{\omega \text{Real}\{n_s(\omega)\}} \left( \pi l - \frac{\phi_1(\omega) + \phi_2(\omega)}{2} \right) \quad (6)$$

The reflection coefficients, and hence their  $\phi_{1,2}(\omega)$  phases, can be readily obtained from mpGMM by considering a mirror of the corresponding material and thickness separating two semi-infinite media: air, and the effective medium characterized by  $n_s(\omega)$ . Then, the solutions for  $L$  in Equation (6) can be found numerically for each value of  $l$  and  $\omega$ , thereby obtaining the mode lines in the  $(L, \omega)$  space.

### 2.3. DFT Implementation

The dipole polarizability matrices  $\alpha_{\nu\nu'}$  used in Equation (3) can be obtained from orbital-based TD-DFT in an ab initio manner without any prior knowledge of the properties of a given or newly designed system. In this section, we will use the indices  $p, q, \dots$  for general orbitals,  $i, j, \dots$  for occupied orbitals and  $a, b, \dots$  for virtual orbitals. To obtain the corresponding dipole polarizabilities for the frequency-dependent perturbations  $\nu$  and  $\nu'$ , that is, an electric or magnetic dipolar field ( $\nu = \{e, m\}$ ), a set of coupled-perturbed Kohn–Sham (CPKS) equations needs to be solved<sup>[34–36]</sup>

$$|\mathbf{x}^\nu, \mathbf{y}^\nu\rangle = -(\Lambda - \omega_\nu \Delta)^{-1} |p^\nu, q^\nu\rangle \quad (7)$$

with the  $2 \times 2$  supermatrices

$$\Lambda = \begin{pmatrix} \mathbf{A} & \mathbf{B} \\ \mathbf{B}^\dagger & \mathbf{A}^* \end{pmatrix}; \Delta = \begin{pmatrix} \mathbb{1} & \mathbf{0} \\ \mathbf{0} & -\mathbb{1} \end{pmatrix} \quad (8)$$

and  $\omega_\nu$  is the frequency of the external perturbation. Furthermore,  $\mathbf{p}^\nu$  and  $\mathbf{q}^\nu$  collect the integrals describing the external electric or magnetic dipolar fields. These integrals are straightforwardly obtained from the electric or magnetic dipole integrals

$$p_{pq}^e = q_{pq}^{e*} = \langle \phi_p | \mathbf{r} | \phi_q^* \rangle \quad (9)$$

$$p_{pq}^m = q_{pq}^{m*} = \frac{i}{2c} \langle \phi_p | (\mathbf{r} - \mathbf{R}) \times \nabla | \phi_q^* \rangle \quad (10)$$

$\mathbf{x}$  and  $\mathbf{y}$  are the vectors obtained by solving Equation (7), and can be interpreted as perturbation coefficients describing the response of the ground-state density to the external perturbation  $\nu$ . In principle, Equation (7) can also be solved for higher-order (quadrupolar or octupolar) contributions by exchanging the right-hand side by the corresponding higher-order electric field integrals. Within the adiabatic approximation and

assuming the perturbation wavelength to be much longer than the size of the nanostructures for which the CPKS equations are solved, the coupling matrices in Equation (8) are given as

$$A_{ia,jb} = (\epsilon_a^{KS} - \epsilon_i^{KS}) \delta_{ij} \delta_{ab} + v_{ia,jb} + f_{ia,jb}^{XC} + K_{ia,jb} \quad (11)$$

$$B_{ia,jb} = v_{ia,bj} + f_{ia,jb}^{XC} + K_{ia,bj} \quad (12)$$

and  $\phi_p$  are the Kohn–Sham (KS) eigenstates obtained from the ground-state KS DFT calculation,  $\epsilon_p^{KS}$  are the corresponding KS orbital energies, and  $v_{pq,rs}$  is an electron-repulsion integral

$$v_{pq,rs} = \int \phi_p(\mathbf{r}) \phi_q(\mathbf{r}) \frac{1}{|\mathbf{r} - \mathbf{r}'|} \phi_r(\mathbf{r}') \phi_s(\mathbf{r}') d\mathbf{r} d\mathbf{r}' \quad (13)$$

$f_{ia,jb}^{XC}$  is the second derivative of the exchange-correlation energy,

$$f_{pq,rs}^{XC} = \frac{\partial^2 E^{XC}}{\partial D_{pq} \partial D_{rs}} \quad (14)$$

with respect to the KS ground-state density matrix  $D_{pq}$ ,

$$D_{pq} = \sum_{\mu\nu} c_p^\mu c_\nu^{q*} \quad (15)$$

$c_p^\mu$  are the solution vectors obtained from solving the Kohn–Sham equations.  $K_{pq,rs}$  is an exchange integral,

$$K_{pq,rs} = \int \phi_p(\mathbf{r}) \phi_q(\mathbf{r}') \frac{a + b \text{erf}(c|\mathbf{r} - \mathbf{r}'|)}{|\mathbf{r} - \mathbf{r}'|} \phi_r(\mathbf{r}) \phi_s(\mathbf{r}') d\mathbf{r} d\mathbf{r}' \quad (16)$$

which is obtained using the seminumerical semiJK algorithm within ref. [22]. Note that  $a, b$ , and  $c$  in Equation (16) are constants defined by the density functional approximation.

The frequency-dependent polarizability tensor  $\alpha_{\nu\nu'}$  is then obtained using the solution vectors  $\mathbf{x}$  and  $\mathbf{y}$  as the direct product

$$\alpha_{\nu\nu'}(\omega) = \langle \mathbf{p}^\nu, \mathbf{q}^\nu | (\Lambda - \omega \Delta^{-1}) | \mathbf{p}^{\nu'}, \mathbf{q}^{\nu'} \rangle = \langle \mathbf{x}^\nu(\omega), \mathbf{y}^\nu(\omega); \mathbf{p}^{\nu'}, \mathbf{q}^{\nu'} \rangle \quad (17)$$

for a given frequency  $\omega$ . Note that  $\omega$  is generally complex for any non-vanishing frequency of interest. Such complex frequency accounts for the finite lifetime of excited states. For each frequency  $\omega$ , one CPKS equation (Equation (7)) needs to be solved for each component of the perturbation  $\nu$ , that is, three Cartesian directions for dipole polarizabilities. Therefore, for  $N$  frequencies,  $3N$  CPKS equations must be solved.

For completeness, we also note that in principle our method is not limited to TD-DFT, but can also be used within the Greens function based GW-Bethe-Salpeter equation framework.<sup>[36,37]</sup>

### 2.4. Effective Material Parameters

For the case of a SURMOF (see Section 4), an isotropic refractive index suitable for use in Equation (6) can be obtained as follows. We start with the general constitutive relations for a molecular anisotropic and homogeneous medium

$$\begin{pmatrix} \mathbf{D} \\ \mathbf{B} \end{pmatrix} = \begin{pmatrix} \epsilon_{\text{eff}} & i\kappa_{\text{eff}}\sqrt{\epsilon_0\mu_0} \\ -i\kappa_{\text{eff}}^T\sqrt{\epsilon_0\mu_0} & \mu_{\text{eff}} \end{pmatrix} \begin{pmatrix} \mathbf{E} \\ \mathbf{H} \end{pmatrix} \quad (18)$$

where  $\mathbf{E}$  and  $\mathbf{H}$  are the external applied electric and magnetic fields, respectively, and  $\mathbf{D}$  and  $\mathbf{B}$  are the average electric displacement and magnetic flux density inside the effective medium, respectively. The material parameters of the medium are the effective permittivity  $\epsilon_{\text{eff}}$ , the effective permeability  $\mu_{\text{eff}}$ , and the effective chirality parameter  $\kappa_{\text{eff}}$ .

For the periodic system of the SURMOF, the values of  $\epsilon_{\text{eff}}$  and  $\mu_{\text{eff}}$  are obtained from the central object in Equation (4)

$$p_{0,\text{tot}} = \left( 1 - T \sum_{R \neq 0} C^{(3)}(-R) e^{ik_0 R} \right)^{-1} T a_0 = T_{\text{eff}} a_0 \quad (19)$$

which we call  $T_{\text{eff}}$  for “effective T-matrix in the lattice”. As explained in ref. [23] (see also ref. [38]),  $T_{\text{eff}}$  collects the multi-scattering response of a unit cell in the lattice. In effect, one can then conceptually equate two systems: On the one hand, the infinite array of interacting unit cells, each characterized by  $T$ , that we have been considering so far, and, on the other hand, an infinite array of non-interacting unit cells, each characterized by  $T_{\text{eff}}$ . In the latter system, it is clear that  $T_{\text{eff}}$  is an excellent object to homogenize materials. That is, given  $T_{\text{eff}}$ , the constitutive parameters of a material are readily derived. An article dedicated to such homogenization strategy is in preparation.<sup>[39]</sup> For the present paper, the connection between  $T_{\text{eff}}$  and  $(\epsilon_{\text{eff}}, \mu_{\text{eff}})$  is obtained as follows. First, we define effective polarizabilities  $\alpha_{\text{vw},\text{eff}}$  by inverting Equation (3) with  $T_{\text{eff}}$  on the left-hand side. We then have that:

$$\begin{aligned} \epsilon_{\text{eff}} &= \epsilon_h \mathbb{1}_3 + \rho \alpha_{\text{ee},\text{eff}} \\ \mu_{\text{eff}} &= \mu_h \mathbb{1}_3 + \rho \alpha_{\text{mm},\text{eff}} \mu_h \end{aligned} \quad (20)$$

where  $\mathbb{1}_3$  is the unit  $3 \times 3$  matrix, and  $\rho$  the concentration of the molecules.

We now make the simplification from anisotropic to isotropic material parameters. There are different ways to compute an isotropic refractive index from anisotropic tensors. We restrict ourselves to a simple method, where the off-diagonal entries of the material parameter tensors are neglected. First, three potentially different refractive indexes are calculated for the diagonal entries of the material parameters,  $n_{\text{vw}} = \sqrt{\epsilon_{\text{r,eff},\text{vw}} \mu_{\text{r,eff},\text{vw}}}$  with  $\epsilon_{\text{r,eff},\text{vw}} = \epsilon_{\text{eff},\text{vw}}/\epsilon_0$  and  $\mu_{\text{r,eff},\text{vw}} = \mu_{\text{eff},\text{vw}}/\mu_0$ . In the second step, these values are averaged to produce a single complex number  $n_{\text{S}} = \frac{1}{3} \sum_{v=1}^3 n_{\text{vw}}$ . Later in the article, we will use the resulting complex effective refractive index for the modal analysis of the joint cavity and SURMOF system using Equation (6). Since the SURMOF under consideration is achiral, we can assume that the averaged  $\kappa_{\text{eff}}$  does not influence the refractive index. We note that, in this paper, we are using the  $T_{\text{eff}}$  corresponding to a 2D lattice for homogenization. As seen below, this provides satisfactory results in our case. The more appropriate approach<sup>[39]</sup> is based on the  $T_{\text{eff}}$  corresponding to a 3D lattice.

For the film of randomly oriented J-aggregates considered in Section 5, we perform a rotational average of the polarizability matrices. These are calculated from the polarizability tensors

from the TD-DFT calculation by diagonalizing the tensors and averaging the resulting diagonal entries. With the Lorenz–Lorentz formulas from ref. [40] the effective permittivity and permeability of the film can be calculated from the rotationally averaged polarizabilities.

### 3. Methodology

The combination of molecular T-matrices with the periodic T-matrix-based solver results in a powerful novel multi-scale methodology to compute the electromagnetic responses of arbitrarily thick films of crystalline or amorphous molecular materials, either isolated, on top of substrates, or inside optical cavities (see Figure 1).

The workflow steps for the more involved crystalline case are explained in detail here below while applying the methodology to a system formed by a SURMOF inside an optical cavity: The system, depicted in Figure 2, consists of a Zn-based Si-Phthalocyanine (Zn-SiPc) SURMOF-2 filling all the space between two planar silver mirrors, and was experimentally studied in ref. [11]. The differences in the workflow for the simpler amorphous case are described in Section 5, where the methodology is applied to an optical cavity filled with a polymer containing randomly oriented molecular J-aggregates, experimentally investigated in for example ref. [29].

The workflow consists of the following six distinguishable steps:

- 1) Structural optimization of the unit cell of the periodic crystalline material using a periodic DFT code;
- 2) Selection of the finite size molecular model of the periodic system;
- 3) Calculation of the complex dynamic polarizability tensors for the selected molecular model;
- 4) Constructing the T-matrices from the dynamic polarizabilities;
- 5) Performing scattering simulations using a periodic Maxwell solver;
- 6) Analyzing the optical properties of the system.

The first step in our workflow is the optimization of the periodic material. For this purpose, we used the CP2K code with settings as described in the Supporting Information. The unit cell was defined by experiments and set to be 21.0 Ångströms in  $\mathbf{a}$  and  $\mathbf{b}$  and 11.0 Ångströms in  $\mathbf{c}$  direction of the lattice vectors.

In the second step, we need to select a finite-size cluster-like molecular model. Here, special care needs to be spent so that the model will lead to the accurate computation of the optical properties of SURMOF thin films. Although the structure of the SURMOF was optimized with a periodic DFT, a cluster-like model is needed to perform TD-DFT calculations of dynamic polarizabilities in the desired spectral range. Calculations of the complex dynamic polarizability elements required to construct the full T-matrix are performed by the Turbomole program. Alongside the standard set of options such as DFT functional, basis set, grid, etc., it is also necessary to fulfill some criteria required by the T-matrix formalism. The calculation of the global response of a cluster of scatterers is based

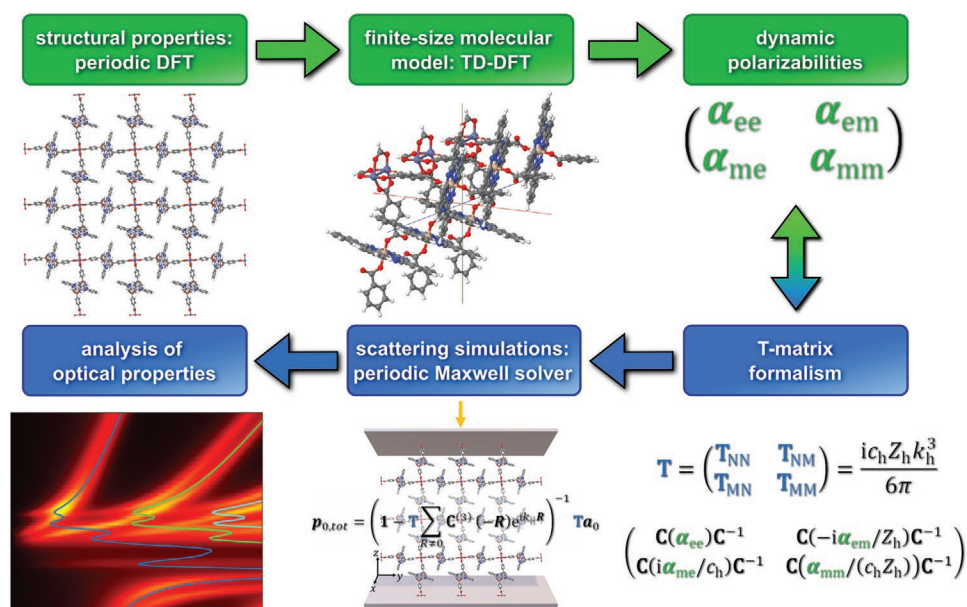


**Figure 1.** Workflow for optical simulations of SURMOF thin films either isolated, on top of substrates, or inside optical cavities. Experimentally observable quantities from optical measurements on devices containing molecular materials can be predicted using quantum light-matter interaction models that fuel rigorous Maxwell scattering theories. The blocks on the quantum-mechanical side (green) are connected to T-matrix-based Maxwell solvers (blue) by a relation between the dynamic polarizabilities of molecular building blocks obtained from ab initio quantum-mechanical simulations, and the T-matrix of such building blocks. This connection enables our multi-scale modeling approach. Instead of SURMOFs, amorphous molecular media such as films containing randomly oriented J-aggregated molecular blocks can be also simulated using a slightly modified workflow where the effective material parameters of the molecular media are derived from the T-matrix of a J-aggregate.

on the assumption that their smallest circumscribing spheres do not overlap.<sup>[41,42]</sup> Nevertheless, accurate results can still be obtained with some small overlap.<sup>[43]</sup> Hence, it is beneficial to choose a molecular model similar to a cube, that is, with sim-

ilar dimensions in all three spatial directions. Additionally, and to minimize edge effects in the computation of dynamic polarizabilities, such cube should be as large as possible considering TD-DFT computational time. In our example, we are modeling

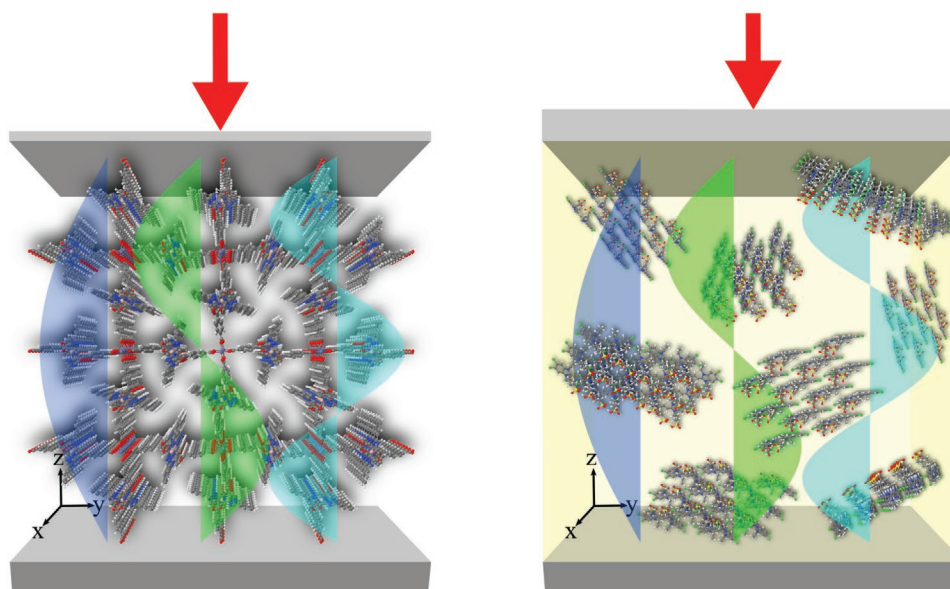


**Figure 2.** Scheme of an illuminated cavity filled with Zn-SiPc-SURMOF-2 (left) and with randomly oriented molecules (right) (not to scale). The cavity consists of two silver mirrors. The top (bottom) mirror has a thickness of 10 (30) nm for the SURMOF-in-cavity system and a thickness of 30 (30) nm for the J-aggregates-in-cavity system. The light propagates along  $-z$  and is launched in from the top. The first three cavity modes are visualized according to the color scheme of the cavity mode lines in Figures 1, 6, 8, and 9.

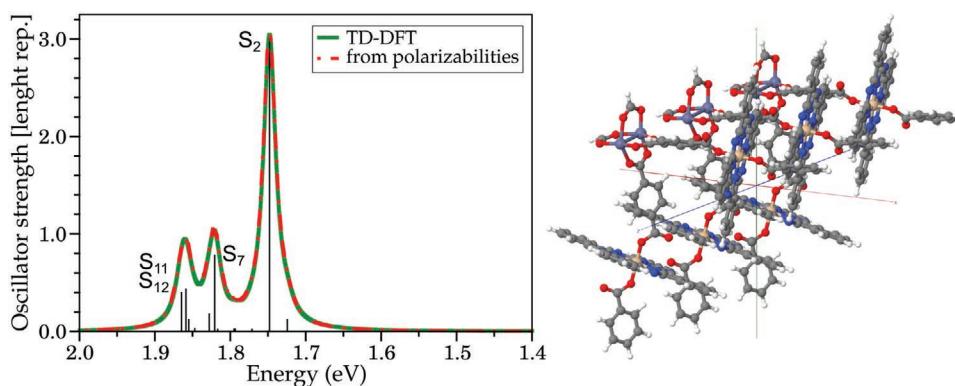


**Figure 3.** Absorption spectrum of the molecular model calculated with the standard TD-DFT approach (full green line), and from dynamic polarizabilities (dashed red line, scaled). Oscillator strengths from TD-DFT calculations (black vertical sticks) are shown in the length representation.

a SURMOF-2 type crystalline thin film consisting of continuously stacked 2D sheets of Zn-paddle wheels (Zn-PWs) and Si-Phthalocyanine (SiPc) linkers along the  $x$ -direction (Figure 2). We tested different molecular models and chose the model composed of 3 Zn-PWs and 3 SiPc linkers in the horizontal and vertical orientation. This molecular model, used in the T-matrix simulations later on in step 5 of the workflow, comprises three unit cells along the stacking direction of the 2D sheets, yielding a total volume of  $21 \times 21 \times 33 \text{ \AA}^3$ . Different molecular models produce similar DFT results at the qualitative level, but quantitative differences impact the quality of optical simulations.

In the third step, we take the chosen molecular model to perform calculations of the dynamic polarizabilities for the discretized excitation energies in the spectral range of interest (618–886 nm in this case). We used a wavelength discretization interval of 2 nm for these simulations. This step is highly parallelized over multiple computational nodes to speed up the expensive TD-DFT calculation for each wavelength. Some sanity checks are in order at this point. First, a standard TD-DFT simulation of the absorption spectrum (green line, Figure 3) of the molecular model representing the periodic SURMOF material is performed. We calculated 20 lowest-lying discrete singlet electronic excitations from the ground state. Those discrete transitions have been broadened with the Lorentzian line shape with full-width at half-maximum of 0.02 eV and visualized in Figure 3. The TD-DFT simulated spectral shape qualitatively resembles the experimentally obtained spectrum of the same SURMOF-2 thin film grown on the surface support.<sup>[11]</sup> The spectrum shows three prominent peaks at 1.75, 1.82, and 1.86 eV. A detailed analysis of leading transitions contributing to the most intense peaks is visualized in Figure S2, Supporting Information. A similar absorption spectrum has been obtained for a simpler molecular model, containing only three vertical linkers without metallic centers (Figure S1, Supporting Information), with only two bands at 1.78 and 1.88 eV. In this case, the band at 1.82 eV is not present, and the lowest energy band is blue-shifted by 0.03 eV. We mostly attribute the better results of the first model to its better compliance with the geometrical criteria explained above. Importantly, in both models, the absorption spectrum constructed from damped dynamic polarizability calculations (dashed red line) has the same

spectral shape, confirming that the calculated polarizability tensors are correct and giving us the confidence to proceed with T-matrix simulations.

In the fourth step, we use Equation (3) to construct T-matrices from the polarizabilities computed with Turbomole. In the next step, T-matrices are fed into mpGMM. In our example, the absorption spectra of the bare Zn-SiPc-SURMOF-2 film and the cavity filled with the film are calculated for different values of the thickness of the film and different values of the energy (frequency) of the incident light. The normal incident plane wave is left-handed circularly polarized. The light is launched from the top, propagating along  $-z$  (Figure 2). The resulting absorption spectra can be seen in Figure 4. All false-color images of 2D arrays in the main text and the Supporting Information, are plotted with UIMAGE.<sup>[44]</sup> The absorption is defined as  $1 - T - R$ , where  $T$  is the transmittance and  $R$  is the reflectance. Figure 4a shows the results for the bare film without the cavity. We observe relatively large absorption between 1.7 and 1.9 eV, consistent with the TD-DFT results in Figure 3. Some resonances are well discernible, but most resonances are spectrally so close to each other that the spectrum shows an indistinct and broad region of high absorption. The absorption spectrum of the cavity filled with the Zn-SiPc-SURMOF-2 displayed in Figure 2 is depicted in Figure 4b. The top silver mirror has a thickness of 10 nm, whereas the bottom silver mirror has a thickness of 30 nm. The values for the permittivity of silver are taken from ref. [45]. We observe in Figure 4b regions of high absorption that are relatively narrow branches, suggesting a direct connection with cavity modes. These branches occur twofold, whereat both branches of each pair are spectrally close but mostly well-distinguishable. In the next section, we show that the twofold occurrence of the branches is related to the anisotropy of the SURMOF film. In the energy range between 1.7 and 1.9 eV, the branches of high absorption of the filled cavity are bent. This bending indicates a coupling of the modes of the empty cavity to the SURMOF resonances, which we also analyze further in the next section.

The SURMOF-in-cavity example shows that the proposed methodology can handle quite complicated systems and that it provides a multi-scale bottom-up link between the molecular scale of quantum mechanical simulations and the device scale. Quantum light-matter interaction models fuel rigorous Maxwell



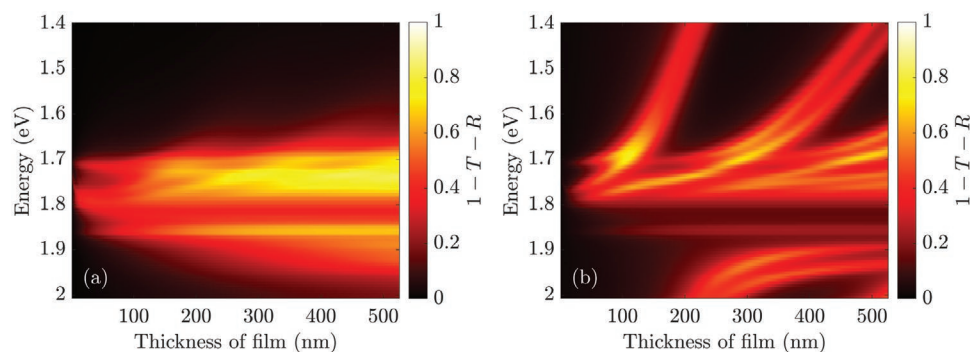


**Figure 4.** a) Absorption spectrum of isolated Zn-SiPc-SURMOF-2 films of different thicknesses (without cavity) and b) of a cavity filled with Zn-SiPc-SURMOF-2 (see Figure 2), as a function of the frequency and the thickness of the film. The incident light is a left-handed circularly polarized plane wave. One can observe in (a) different resonances of the SURMOF between 1.7 and 1.9 eV. In the entire spectrum of the filled cavity in (b), the regions of high absorption occur as relatively narrow branches related to cavity modes. The modes are bent in the energy range between 1.7 and 1.9 eV due to the SURMOF resonances. Additionally, we observe in (b) that every region of high absorption occurs twofold. The branches of most pairs are narrowly spaced but well distinguishable. The twofold occurrence of the branches is due to the anisotropy of the SURMOF film.

scattering theories for predicting any optical measurement on the considered device. It is worth mentioning that, while in all the results included in the main text, the illumination is a plane wave at normal incidence, the periodic solver allows for arbitrary incidence angles (see Figure S6, Supporting Information). Therefore, and using the superposition principle, the response to general incident beams can also be obtained. In the next section, we analyze the results for the Zn-SiPc-SURMOF-2-in-cavity system in more detail.

#### 4. Zn-SiPc-SURMOF-2 Inside the Optical Cavity

In Figure 4b, we observe that each cavity mode has two spectrally very close branches in the absorption spectrum for incident left-handed circularly polarized light. Further simulations in **Figure 5** indicate that this is due to the anisotropy of the molecular film: In this particular SURMOF-2, the spacing between molecules in the  $x$ -direction is almost two times smaller than in the  $y$ -direction. We show in Figure 5

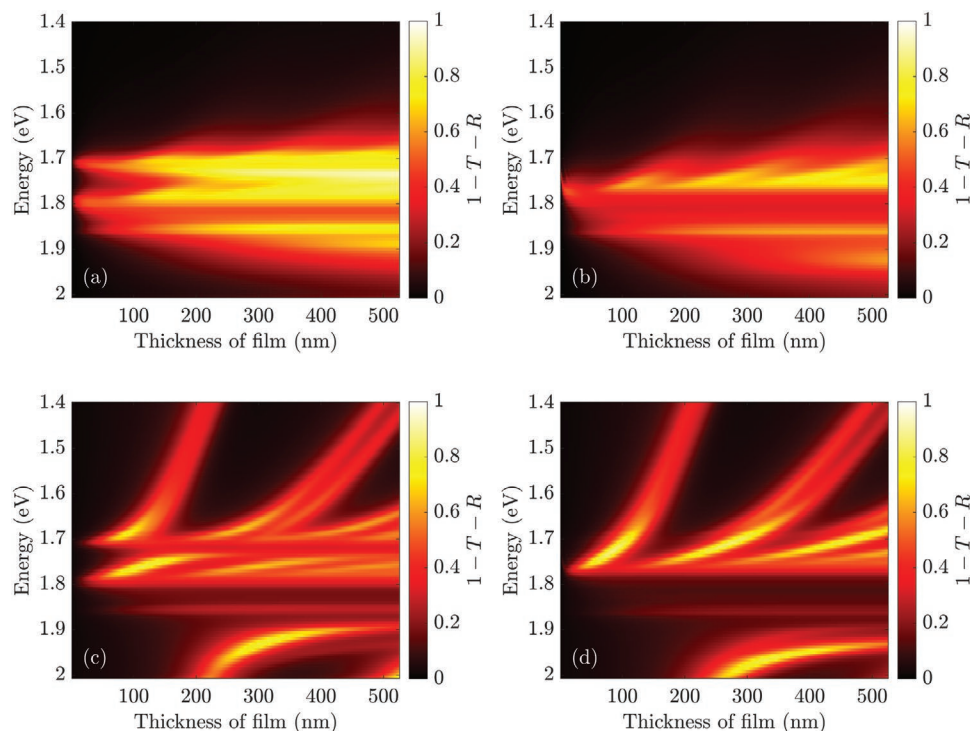


**Figure 5.** a,b) Absorption spectra of Zn-SiPc-SURMOF-2 without cavity and of c,d) a cavity filled with Zn-SiPc-SURMOF-2 for incident TE- and TM-polarized light, as a function of the frequency and the thickness of the film. Due to the SURMOF anisotropy, the absorption spectra with and without the cavity differ depending on the incident linear polarization. The intensity of the branches belonging to the same cavity mode, for instance, is different for TE- and TM-polarized light, respectively.

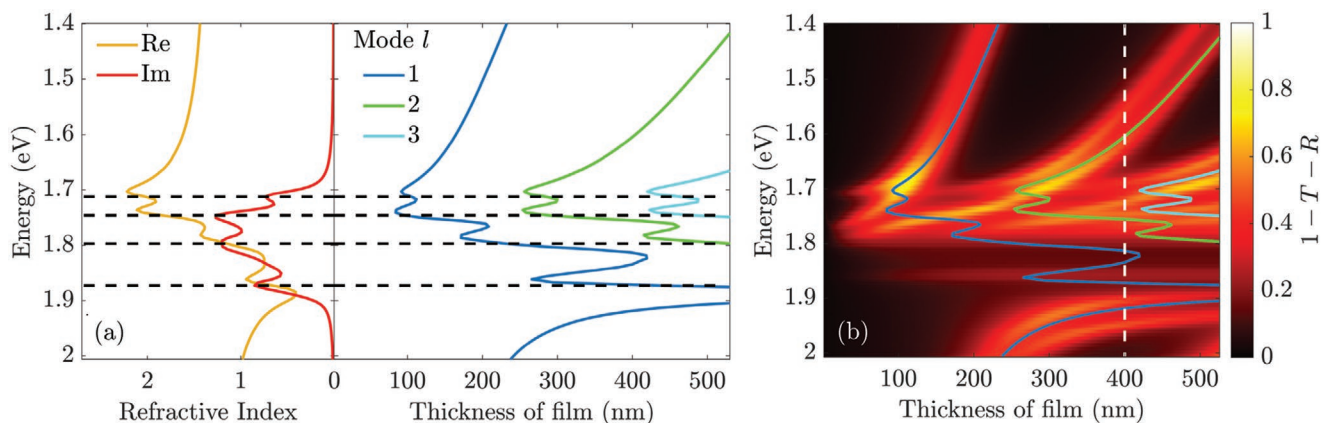


**Figure 6.** a) Effective refractive index of Zn-SiPc-SURMOF-2 and b) absorption of filled cavity, both including the computed cavity mode lines. The effective refractive index calculated with the effective T-matrix is highly dispersive. Furthermore, the real part of the refractive index reaches values above 2. As a consequence, not only one mode but four cavity modes and also different regions of bending are observable in (a). These cavity modes agree well with the regions of high absorption of the filled cavity in (b).

the absorption spectra for incident linearly polarized light for both the SURMOF without the cavity (Figure 5a,b) and the cavity filled with the SURMOF (Figure 5c,d). TE-polarization denotes a polarization along the y-axis, and TM polarization denotes a polarization along the x-axis. We observe that both systems absorb incident TE- and TM-polarized light differently. Regarding the filled cavities in Figure 5c,d, some modes still occur twofold, as for circular polarization. Yet, the branches of a specific mode have different intensities, depending on the incident linear polarization. For instance, on the first cavity mode for high energies, the absorption on each of the two branches is much larger for either the TE- or the TM- polarization. It is roughly twice as large as for the case of circular polarization in Figure 4b. The distinction between the TE and TM absorption in other lines is not as marked but still visible. Since the principal axes of the SURMOF film do not coincide with the  $x$ -,  $y$ -, and  $z$ -axes, we do not expect the modes to be purely TE- or TM-polarized, so each linear polarization can still excite both branches in each line, albeit with different strength. These effects, however, might not be observed in an experiment, since in a conventional setup, the absorption of larger areas of coated substrates is detected. Within these larger areas, different orientations of the SURMOF structure typically exist, which can cancel effects depending on the incident polarization. Nevertheless, the observation of anisotropic effects in the simulations indicates an accurate detection of the arrangement of the molecules and their influence on the optical properties.

After elucidating the origin of the double-line features, let us turn our attention to the overall structure of the absorption lines. We use the effective isotropic refractive index  $n_s$  derived from the  $\mathbf{T}_{\text{eff}}$  of the SURMOF as explained in Section 2.4, and perform a mode analysis, as explained in Section 2.2. **Figure 6a** shows the modal lines together with the real and imaginary parts of  $n_s$ . **Figure 6b** shows the mode lines overlaid on top of the calculated absorption. The presence of the SURMOF produces a complicated mode landscape, particularly in the energy region where the molecules absorb the most. For example, the  $l = 1$  mode shown as the blue mode line in **Figure 6a**, can be seen to be split by the region of molecular

absorption. Nevertheless, except for the double-line features that we have decided to remove from this analysis, the match between the theoretical prediction of the mode position and the position of the calculated absorption lines is very satisfactory. It allows to assign mode labels to the absorption lines. Such assignment provides crucial information for the refined interpretation of the results from ref. [11]. The two peaks seen for  $L = 400$  nm around 1.9 and 1.55 eV in **Figure 2c** of ref. [11], do not correspond to the splitting of a single mode. Rather, as the cuts between the mode lines and the vertical dashed line at  $L = 400$  nm in **Figure 6b** show, each peak corresponds to a different mode:  $l = 1$  on the higher energy peak and  $l = 2$  on the lower energy peak.

We now study an optical cavity filled with a polymer containing a molecular J-aggregate, which illustrates the application of the multi-scale approach to amorphous molecular films, where the molecular blocks are randomly oriented.

## 5. J-Aggregate of TDBC Embedded in a PVA Polymer within An Optical Cavity

We study the molecule-light coupling of 5,6-dichloro-2-[[5,6-dichloro-1-ethyl-3-(4-sulphobutyl)benzimidazol-2-ylidene]propenyl]-1-ethyl-3-(4-sulphobutyl) benzimidazolium hydroxide (in short TDBC) embedded into a polyvinyl alcohol (PVA) polymer, and inside a cavity similar to the cavity of the first example. Opto-physical properties of this system have been experimentally studied multiple times.<sup>[29,46–48]</sup> In particular, it was experimentally observed that the characteristic absorption peak of a thin film of a TDBC J-aggregate at  $\approx 2.14$  eV ( $\approx 580$  nm) is split into two peaks at  $\approx 2.25$  eV ( $\approx 550$  nm) and  $\approx 1.91$  eV ( $\approx 650$  nm) upon placing the film inside an optical cavity formed by two planar silver mirrors.<sup>[29]</sup> However, theoretical simulations of the J-aggregate of this molecule are sparse.<sup>[49]</sup>

Steps 1 and 2 of the workflow described in Section 3 are different in this example since the polymer embedded TDBC is not a crystalline material. Instead of performing periodic DFT optimization of the system, a neutral *cis*-TDBC molecule

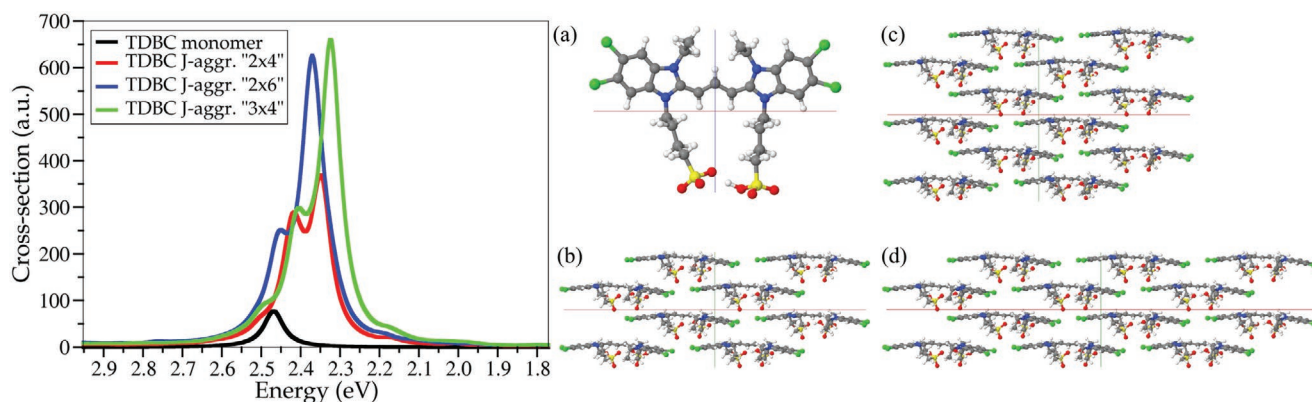


**Figure 7.** a) Absorption spectra of the *cis*-TDBC monomer as well as b–d) different molecular models of a brickstone lattice of 2D J-aggregates of TDBC (“2 × 4”, “2 × 6”, and “3 × 4”) embedded into a COSMO implicit model of a mixture of polyvinyl alcohol (PVA) polymer and water (95/5 wt%) calculated, from dynamic polarizabilities. The cross-section is reported in atomic units.

within a polarizable continuum implicit solvation model for a mixture of 95/5 wt% of PVA/H<sub>2</sub>O was optimized as a first step (Figure 7a). The local minimum character of the optimized geometry was confirmed by the calculation of vibrational modes. In the following step, the optimized geometry of TDBC was used to construct a brickstone lattice of a 2D J-aggregate in three different molecular models named “2 × 4”, “2 × 6”, and “3 × 4” containing 8 and 12 molecules respectively, as depicted in Figure 7b–d. Lattice parameters of  $L_x = 20.48 \text{ \AA}$  and  $L_y = 4.6 \text{ \AA}$  were used, as described in Guzik et al.<sup>[49]</sup>

Steps 3 and 4 are the same as in the previous example: Complex dynamic polarizability tensors for electric–electric, electric–magnetic and magnetic–magnetic sub-tensors for the TDBC J-aggregate models in a conductor-like screening model (COSMO) PVA/H<sub>2</sub>O implicit surrounding were calculated for discrete energy points with 1 nm step covering the range of 420–700 nm. T-matrices were constructed from these polarizabilities as described above. All theoretical details of the quantum simulations are provided in the Supporting Information. Figure 7 shows the absorption spectra of the TDBC monomer (Figure 7a) and of the molecular models of TDBC 2D J-aggregates consisting of 8 and 12 molecules (Figure 7b–d) packed in a brickstone lattice from the first-principle TD-DFT simulations. The absorption of the monomer molecule in the COSMO PVA/H<sub>2</sub>O surrounding exhibits only one peak from a single electronic excitation transition at 2.47 eV (502 nm) rising from the transition between the highest to the lowest unoccupied molecular orbitals with a total contribution of 97% (Figure 7a; Figure S3, Supporting Information). Two J-aggregate models (Figure 7b,c) shows a double absorption peak, red-shifted with respect to the monomer, lying between 2.35 and 2.45 eV, with the higher energy peak being more pronounced. The analysis of the discrete electronic transitions for the most intensive peaks of the “2 × 4” model clearly shows that the spectrum of the J-aggregates arises from the collective excitations of all molecules within the molecular model/s (Figure S4, Supporting Information). For the larger “2 × 6” model, the high energy peak is less pronounced, while the low energy peak becomes significantly dominant. In the case of the “3 × 4” model (Figure 7d), the spectrum is furthermore red-shifted by  $\approx 0.05 \text{ eV}$  ( $\approx 10 \text{ nm}$ ). From these models, it follows

that for the theoretical description of the absorption spectra of 2D J-aggregates, it is important to have a molecular model as large as possible in both *x*- and *y*-direction. A larger model in *x*-direction would further red-shift the spectrum to the correct position. Moreover, having additional aggregated molecules in TD-DFT simulations also increases the overall intensity of the absorption. Extrapolation of this trend to the limit of thousands of molecules stacked in the 2D J-aggregate indicates that the lower energy peak would become the only observable feature of the spectrum, which is in the agreement with previous experimental measurements.<sup>[29,46–48]</sup>

For the Maxwell simulations of step 5, the molecular film containing a mixture of randomly oriented J-aggregate structures is effectively modeled as an isotropic and homogeneous slab. The effective material parameters of the slab are calculated as described in Section 2.4. We choose as concentration of the J-aggregates in the film  $n = 10^{20} \text{ cm}^{-3}$ , which is estimated for the experiment in ref. [29]. For the model “3 × 4” considered in the main part, this leads to a concentration of  $n = \frac{1}{12} 10^{20} \text{ cm}^{-3}$ . In the Supporting Information, we also consider the results for the “2 × 4” and “2 × 6” models, which are very similar. According to the experimental setup in ref. [29], the film is placed in a cavity formed between two planar silver mirrors with a thickness of 30 nm.

Figure 8 shows the absorption and modal analysis for the J-aggregate system, analogous to Figure 6 for the SURMOF. The effective refractive index shown in Figure 8a allows on the one hand to compute the thickness and frequency dependent absorption using mpGMM (see Figure 8b), and, on the other hand, to compute the modal lines for the joint molecules plus cavity system. We observe that the modal lines here are much less deformed than in the SURMOF case. In particular, the vertical white dashed line shown in Figure 8b, which corresponds to the experimentally chosen<sup>[29]</sup> thickness of 145 nm, only crosses high absorption areas belonging to the  $l = 1$  mode. The absorption area at higher energies, however, is at the position of the material resonance for this thickness. Therefore, the white line does not cross the blue mode line. As we show in Figure S9, Supporting Information, a more appropriate thickness is 120 nm for which the splitted absorption peaks of the

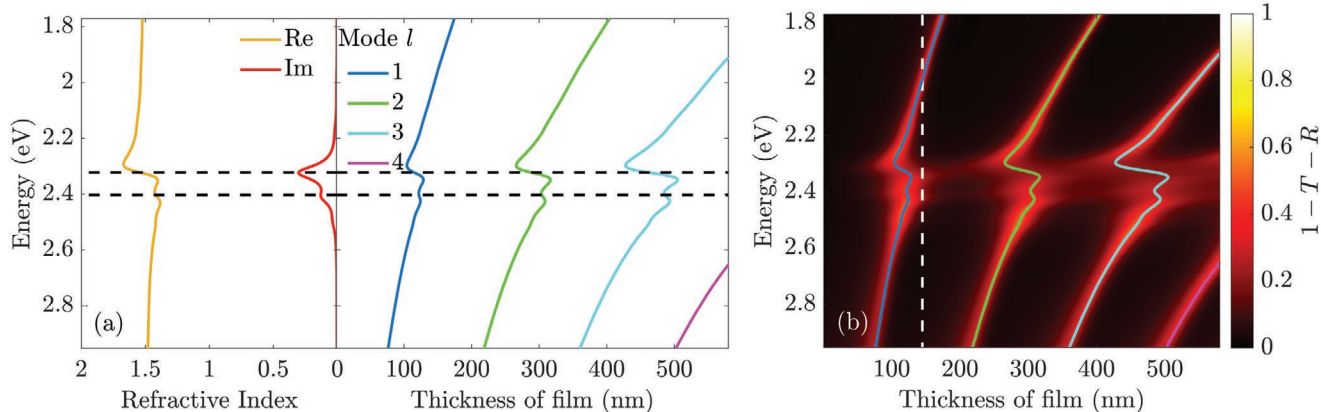


**Figure 8.** a) Effective refractive index of J-aggregate film and b) absorption of filled cavity with mode analysis. Given a value of the thickness of the film, a frequency scan encounters absorption peaks belonging to the same mode, in contrast to Figure 6. This is related to a smaller difference of the refractive index for the energy values lower and higher than the material resonance of the J-aggregate.

filled cavity are on both sides of the material resonance. This is the situation observed in ref. [29]. The shift in comparison to the experiment can be caused by a possible different value of the concentration in ref. [29] which is only estimated, and by the fact that TD-DFT shows a shifted value of the material resonance in Figure 7. We then deduce that the absorption peaks measured in ref. [29] correspond to the same mode, in contrast to the conclusion in the case of the SURMOF. This qualitative difference between the two systems can be explained by comparing the effective refractive index of both samples, depicted in Figures 6a and 8a, respectively. In the SURMOF, the difference between the refractive index for energies higher and lower than its resonance frequencies is much higher than in the J-aggregate film. This leads to a more pronounced deformation of the modal lines of the SURMOF-in-cavity system, which increase the chance of crossing two different modes when scanning the frequency for some given thickness. This explanation is confirmed by artificially increasing the concentration of the J-aggregates in the film by a factor of five. Then, the refractive index becomes both larger and considerable different for energies higher and lower than the resonance frequency

(see Figure 9a). Figure 9b shows that, with the higher concentration, the situation is closer to the case of the SURMOF-in-cavity system. Increasing the concentration of the J-aggregates is a useful theoretical handle for understanding the differences between the two systems that we have studied, independently of whether such concentration can be achieved in practice or not.

Finally, we note that, if desired, the molecular concentration in the SURMOF structure can be decreased by increasing the length of the linkers,<sup>[33]</sup> which results in increased lattice constants.

## 6. Discussion

In this section, we briefly discuss the main limitations of our approach.

One limitation of mpGMM is that two different 2D-lattices cannot co-exist in the same system. For example, a MOF film and an array of silicon disks, or two MOF films with different lattices. This limitation can be solved by extending mpGMM to include anisotropic and homogeneous slabs, and treating the

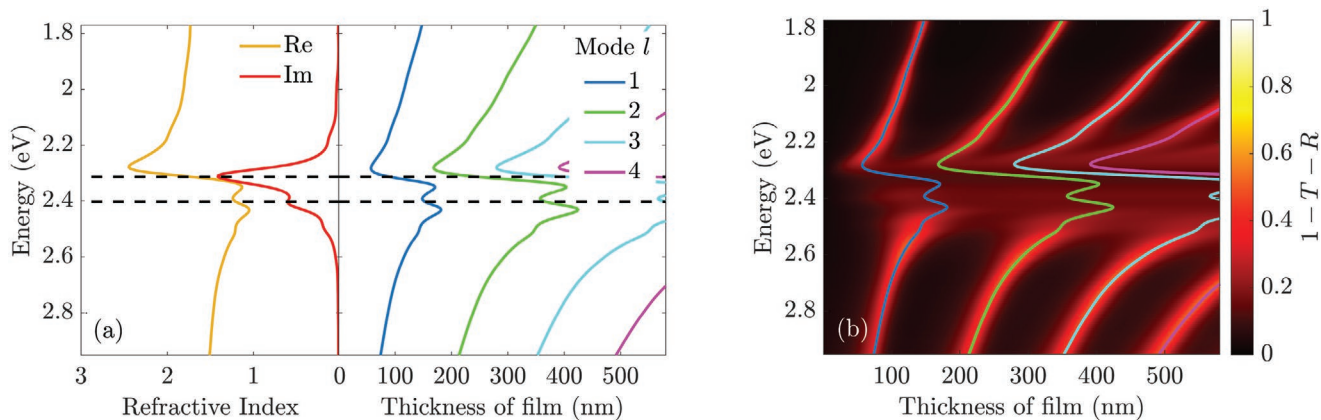


**Figure 9.** a) Effective refractive index of J-aggregate film and b) absorption of filled cavity with mode analysis for an increase of the concentration of the molecules by a factor of five. As the difference of the refractive index on both sides of the material resonance is increased, one can observe peaks belonging to two different cavity modes by scanning the frequency with a fixed thickness.

MOF films as a material with effective anisotropic constitutive relations. Another limitation is the current restriction to dipolar responses for the molecular unit blocks. While the dipolar approximation is typically very good in light-molecule interaction, the restriction can be removed by computing higher order terms such as quadrupoles with TD-DFT, and translating them into the T-matrix formalism.

Regarding computational time, the TD-DFT simulations are the bottleneck in the proposed multi-scale approach. In particular, for periodic media one needs, on the one hand, to take the largest possible molecular unit cell for minimizing edge effects and including all relevant features, but on the other hand, we want to obtain dynamic polarizabilities in a reasonable time. The computational walltimes are defined by the system size together with the chosen DFT functional, quality of the basis set, and available computational resources. From our experience, at the moment, it is possible to perform calculations of dynamic polarizabilities with satisfactory quality in a reasonable time frame for around 1000 atoms for the visible part of the electromagnetic spectrum, and up to 800 atoms for the UV part of the spectrum. We expect these computational limits to improve thanks to the constant improvements in DFT algorithms and computational capabilities.

Finally, the methodology does not include the possible chemical interaction between the atoms of the cavity walls and the molecules in their immediate vicinity. These effects could be important in very thin cavities, but the cavities used in experiments are thick enough so that the proportion of molecules near the cavity walls is very small, and these effects can be safely neglected.

## 7. Conclusions and Outlook

We have presented a multi-scale approach that, starting from ab initio quantum mechanical molecular simulations, can compute the electromagnetic response of macroscopic photonic devices containing molecular materials. The approach is versatile and general. As exemplary applications, we have used the methodology to analyze the absorption of optical cavities filled with either a Zn-SiPc-SURMOF-2, or J-aggregates. The simulated spectra for the SURMOF show effects due to the anisotropy of the SURMOF film. The analysis allows to identify which joint light-matter modes are responsible for the different absorption lines of the systems, showing that as the molecular concentration increases, so does the modulation of the effective refractive index of the medium in the cavity, which then leads to a more pronounced bending of the modal lines. For frequency scans at a fixed cavity thickness, increasing the bending increases the energy difference between two peaks of the same mode, and can also cause the detection of peaks belonging to two different modes. The dependence of the two effects with the concentration can be readily computed using our multiscale methodology.

The approach presented here will be a very useful tool for the computer-aided design and optimization of the optical properties of devices containing molecular materials, and for the interpretation of experimental measurements. We also foresee that the ability to make calculations combining complex optical

cavities with complex molecular materials can be of help in the booming field of polaritonic chemistry.

## Supporting Information

Supporting Information is available from the Wiley Online Library or from the author.

## Acknowledgements

M.K., D.B., C.W., and C.R. acknowledge support by the Deutsche Forschungsgemeinschaft (DFG, German Research Foundation) under Germany's Excellence Strategy via the Excellence Cluster 3D Matter Made to Order (EXC-2082/1-390761711) and from the Carl Zeiss Foundation via the CZF-Focus@HEiKA Program. M.K., C.H., and C.R. acknowledge funding by the Volkswagen Foundation. I.F.C., C.W., and C.R. acknowledge support by the Helmholtz Association via the Helmholtz program "Materials Systems Engineering" (MSE). B.Z. and C.R. acknowledge support by the KIT through the "Virtual Materials Design" (VIRTMAT) project. M.K. acknowledges support by the state of Baden-Württemberg through bwHPC and the German Research Foundation (DFG) through grant no. INST 40/575-1 FUGG (JUSTUS 2 cluster) and the HoreKa supercomputer funded by the Ministry of Science, Research and the Arts Baden-Württemberg and by the Federal Ministry of Education and Research.

Open access funding enabled and organized by Projekt DEAL.

## Conflict of Interest

The authors declare no conflict of interest.

## Data Availability Statement

The data that support the findings of this study are available from the corresponding author upon reasonable request.

## Keywords

J-aggregates, multi-scale approach, optical cavities, surface metal-organic frameworks, time-dependent density-functional theory, transition matrix formalism

Received: January 12, 2022

Revised: March 17, 2022

Published online:

- [1] S. L. James, *Chem. Soc. Rev.* **2003**, 32, 276.
- [2] J.-L. Zhuang, A. Terfort, C. Wöll, *Coord. Chem. Rev.* **2016**, 307, 391.
- [3] R. Gao, M. S. Kodaimati, D. Yan, *Chem. Soc. Rev.* **2021**, 50, 5564.
- [4] T. Viswanathan, M. Gopalakrishnan, K. Thirumoorthy, M. Prakash, N. Palanisami, *J. Phys. Chem. C* **2021**, 125, 8732.
- [5] Y. Wang, W. Fang, M. Bhowmick, C. Sun, Z. Men, *Appl. Phys. Lett.* **2021**, 118, 121102.
- [6] J. Feis, D. Beutel, J. Köpfler, X. Garcia-Santiago, C. Rockstuhl, M. Wegener, I. Fernandez-Corbaton, *Phys. Rev. Lett.* **2020**, 124, 033201.
- [7] P. Scott, X. Garcia-Santiago, D. Beutel, C. Rockstuhl, M. Wegener, I. Fernandez-Corbaton, *Appl. Phys. Rev.* **2020**, 7, 041413.

- [8] D. Beutel, P. Scott, M. Wegener, C. Rockstuhl, I. Fernandez-Corbaton, *Appl. Phys. Lett.* **2021**, *118*, 221108.
- [9] M. Oldenburg, A. Turshatov, D. Busko, S. Wollgarten, M. Adams, N. Baroni, A. Welle, E. Redel, C. Wöll, B. S. Richards, I. A. Howard, *Adv. Mater.* **2016**, *28*, 8477.
- [10] J. Fregoni, F. J. García-Vidal, J. Feist, *arXiv:2111.08394*, **2021**.
- [11] R. Haldar, Z. Fu, R. Joseph, D. Herrero, L. Martín-Gomis, B. S. Richards, I. A. Howard, A. Sastre-Santos, C. Wöll, *Chem. Sci.* **2020**, *11*, 7972.
- [12] M. Rödel, P. Lisinetskaya, M. Rudloff, T. Stark, J. Manara, R. Mitric, J. Pflaum, *arXiv:2111.09185*, **2021**.
- [13] M. Malerba, M. Jeannin, P. Goulain, A. Bousseksou, R. Colombelli, J.-M. Manceau, *arXiv:2108.02433*, **2021**.
- [14] A. Thomas, J. George, A. Shalabney, M. Dryzhakov, S. J. Varma, J. Moran, T. Chervy, X. Zhong, E. Devaux, C. Genet, J. A. Hutchison, T. W. Ebbesen, *Angew. Chem., Int. Ed.* **2016**, *55*, 11462.
- [15] F. J. Garcia-Vidal, C. Ciuti, T. W. Ebbesen, *Science* **2021**, *373* eabd0336.
- [16] D. S. Wang, S. F. Yelin, *ACS Photonics* **2021**, *8*, 2818.
- [17] D. G. Baranov, M. Wersaäll, J. Cuadra, T. J. Antosiewicz, T. Shegai, *ACS Photonics* **2018**, *5*, 24.
- [18] D. S. Dovzhenko, S. V. Ryabchuk, Y. P. Rakovich, I. R. Nabiev, *Nanoscale* **2018**, *10*, 3589.
- [19] Z. Jiang, A. Ren, Y. Yan, J. Yao, Y. S. Zhao, *Adv. Mater.* **2022**, *34*, 2106095.
- [20] A. D. Sample, J. Guan, J. Hu, T. Reese, C. R. Cherqui, J.-E. Park, F. Freire-Fernández, R. D. Schaller, G. C. Schatz, T. W. Odom, *Nano Lett.* **2021**, *21*, 7775.
- [21] P. A. Thomas, K. S. Menghrajani, W. L. Barnes, *J. Phys. Chem. Lett.* **2021**, *12*, 6914.
- [22] C. Holzer, *J. Chem. Phys.* **2020**, *153*, 184115.
- [23] D. Beutel, A. Groner, C. Rockstuhl, I. Fernandez-Corbaton, *J. Opt. Soc. Am. B* **2021**, *38*, 1782.
- [24] I. Fernandez-Corbaton, D. Beutel, C. Rockstuhl, A. Pausch, W. Klopfer, *ChemPhysChem* **2020**, *21*, 878.
- [25] P. Waterman, *Proc. IEEE* **1965**, *53*, 805.
- [26] M. I. Mishchenko, *J. Quant. Spectrosc. Radiat. Transfer* **2020**, *242*, 106692.
- [27] N. Stefanou, V. Yannopapas, A. Modinos, *Comput. Phys. Commun.* **2000**, *132*, 189.
- [28] M. Nečada, P. Törmä, *Commun. Comput. Phys.* **2021**, *30*, 357.
- [29] T. Schwartz, J. A. Hutchison, J. Léonard, C. Genet, S. Haacke, T. W. Ebbesen, *ChemPhysChem* **2013**, *14*, 125.
- [30] B. S. Simpkins, K. P. Fears, W. J. Dressick, B. T. Spann, A. D. Dunkelberger, J. C. Owrutsky, *ACS Photonics* **2015**, *2*, 1460.
- [31] C. Climent, J. Feist, *Phys. Chem. Chem. Phys.* **2020**, *22*, 23545.
- [32] I. Fernandez-Corbaton, *Ph.D. Thesis*, Macquarie University, **2014**.
- [33] J. Liu, B. Lukose, O. Shekhah, H. K. Arslan, P. Weidler, H. Gliemann, S. Bräse, S. Grosjean, A. Godt, X. Feng, K. Müllen, I.-B. Magdau, T. Heine, C. Wöll, *Sci.Rep.* **2012**, *2*, 921.
- [34] R. Bauernschmitt, R. Ahlrichs, *Chem. Phys. Lett.* **1996**, *256*, 454.
- [35] F. Furche, *J. Chem. Phys.* **2001**, *114*, 5982.
- [36] M. Kehry, Y. J. Franzke, C. Holzer, W. Klopfer, *Mol. Phys.* **2020**, *118*, e1755064.
- [37] Y. J. Franzke, C. Holzer, F. Mack, *J. Chem. Theory Comput.* **2022**, *18*, 1030.
- [38] A. Rahimzadegan, T. D. Karamanos, R. Alaei, A. G. Lamprianidis, D. Beutel, R. W. Boyd, C. Rockstuhl, *arXiv: 2108.12364*, **2021**.
- [39] B. Zerulla, R. Venkitakrishnan, D. Beutel, M. Krstić, C. Holzer, C. Rockstuhl, I. Fernandez-Corbaton, unpublished.
- [40] A. Sihvola, I. Lindell, *J. Electromagn. Waves Appl.* **1992**, *6*, 553.
- [41] B. Peterson, S. Ström, *Phys. Rev. D* **1973**, *8*, 3661.
- [42] M. I. Mishchenko, L. D. Travis, D. W. Mackowski, *J. Quant. Spectrosc. Radiat. Transfer* **1996**, *55*, 535.
- [43] D. Schebarchov, E. C. L. Ru, J. Grand, B. Auguié, *Opt. Express* **2019**, *27*, 35750.
- [44] Frederic Moisy, UIMAGE-UIMAGESC, MATLAB Central File Exchange, <https://www.mathworks.com/matlabcentral/fileexchange/11368-uimage-uimagesc> (accessed: March 2021).
- [45] Y. Jiang, S. Pillai, M. A. Green, *Sci. Rep.* **2016**, *6*, 30605.
- [46] E. S. H. Kang, S. Chen, S. Sardar, D. Tordera, N. Armakavicius, V. Darakchieva, T. Shegai, M. P. Jonsson, *ACS Photonics* **2018**, *5*, 4046.
- [47] S. B. Anantharaman, J. Kohlbrecher, G. Rainó, S. Yakunin, T. Stöferle, J. Patel, M. Kovalenko, R. F. Mahrt, F. A. Nüesch, J. Heier, *Adv. Sci.* **2021**, *8*, 1903080.
- [48] D. M. Coles, N. Somaschi, P. Michetti, C. Clark, P. G. Lagoudakis, P. G. Savvidis, D. G. Lidzey, *Nat. Mater.* **2014**, *13*, 712.
- [49] S. Valleau, S. K. Saikin, M.-H. Yung, A. A. Guzik, *J. Chem. Phys.* **2012**, *137*, 034109.